

Research Article

Modal Analysis for a Rod-Fastened Rotor considering Contact Effect Based on Double Fractal Model

Yang Liu ^{1,2}, Qi Yuan ^{1,2}, Pu Li^{1,2} and Guangyu Zhu^{1,2}

¹School of Energy and Power Engineering, Xi'an Jiaotong University, Xi'an 710049, China

²Shaanxi Engineering Laboratory of Turbomachinery and Power Equipment, Xi'an 710049, China

Correspondence should be addressed to Qi Yuan; qyuan@xjtu.edu.cn

Received 28 January 2019; Accepted 28 March 2019; Published 2 May 2019

Academic Editor: Marcello Vanali

Copyright © 2019 Yang Liu et al. This is an open access article distributed under the Creative Commons Attribution License, which permits unrestricted use, distribution, and reproduction in any medium, provided the original work is properly cited.

The rod-fastened rotor is the core component of the gas turbine. It comprises several discs and tie rods. The flexural stiffness of the contact interface is the key factor for rotordynamic analysis. The contact interfaces of the discs are usually manufactured by grinding. The measured contour curve of the contact interfaces of an experimental rod-fastened rotor is analyzed by the structural function method, which shows that the contact interfaces can be well described by the double fractal model with fractal dimensions D_1 and D_2 and the fractal roughness parameters G_1 and G_2 . The Hertz model is used to analyze the contact of the single asperity on the contact interface. On this basis, the flexural stiffness of the contact interface considering the pretightening force and the bending moment is derived. Modal frequencies of the experimental rod-fastened rotor under different pretightening forces and the bending moment (caused by gravity) are obtained by three-dimensional finite element analysis and experimental modal tests. It is observed that the modal frequencies increase with the nominal pressure of the contact interface, and the experimental results are consistent with the calculated results.

1. Introduction

The rod-fastened rotors are widely used in aeroengines and heavy-duty gas turbines (see Figure 1). In order to avoid the damage caused by flexural vibration, it is necessary to accurately calculate the flexural vibration modal frequencies of the gas turbine rotor at the design stage. Because the rotor is not a continuous whole, the contact effect between two discs has a great influence on the dynamic characteristics. There are some researches about the dynamic performance of such structures. Klompas [1] analyzed the influence of the bending moment on the dynamic characteristic of the rotor joints in the turbomachine. Lee and Lee [2] investigated the effect of the central tie rod on the rotordynamic performances of an auxiliary power unit gas turbine rotor. Lu et al. [3] calculated the modal frequencies of a rod-fastened rotor subjected to different pretightening forces by the three-dimensional finite element method. Liu et al. [4] studied the dynamic stability of a rod-fastened rotor bearing system considering the nonuniform pretightening forces. However,

the effect of the contact stiffness on the dynamic characteristic of the rod-fastened rotor was not considered.

For the contact stiffness of the contact interface, some researchers have studied the contact stiffness in microscale. Rao et al. [5] calculated the contact stiffness using the Hertz elastic contact theory and Greenwood-Williamson statistical model. He et al. [6] studied the contact stiffness of rough contact interfaces using Greenwood-Williamson model and the elastic-plastic contact model. Zhang et al. [7] identified the contact stiffness by modal test and obtained the relationship between the contact stiffness and the pretightening force. There are also some researches to analyze the flexural stiffness considering the bending moment. Isa et al. [8] established a bilinear stiffness model to calculate the flexural stiffness of a rod-fastened rotor subjected to the bending moment. Gao et al. [9] studied the effect of the bending moment and the pretightening force on the flexural stiffness of the contact interface in the rod-fastened rotor. Several researchers calculated the equivalent stiffness of bolted structures by the finite element method. Lehnhoff

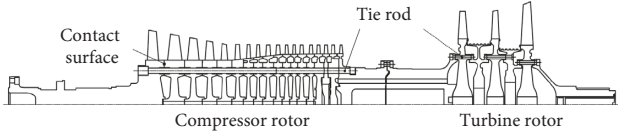


FIGURE 1: Typical structure of the rod-fastened rotor.

et al. [10, 11] calculated the equivalent stiffness of the bolted joints using the axisymmetric finite element model. Yuan et al. [12] calculated the contact stiffness and flexural stiffness of the gas turbine rotor with curvic couplings using the three-dimensional finite element model.

In the above studies, the contact stiffness is calculated using Greenwood–Williamson statistical model. However, the contact interfaces of the discs in the actual gas turbine are manufactured by grinding. Due to the different scales of plastic deformation and microfracture during processing, such machined surfaces generally have double fractal characteristic [13]. Jiang et al. [14] calculated the normal contact stiffness of the joint surface based on the fractal model and compared the theoretical calculation results with the experimental data. Buczkowski et al. [15] used the Weierstrass–Mandelbrot function to express the fractal features of the rough surface and calculated the normal contact stiffness of the isotropic rough surface during extrusion deformation.

However, there are few investigations that focus on the analysis of the flexural stiffness of the rod-fastened rotor, considering the pretightening force and the bending moment based on double fractal model. In this paper, an experimental rod-fastened rotor is designed. The contact interfaces of the rotor are grinding. The contour curve of the contact interfaces is analyzed by the structural function method, which shows that the contact interfaces have double fractal characteristic. The normal contact stiffness of the contact interface is obtained by the Hertz contact theory and the double fractal model. The flexural stiffness of the contact interface considering the pretightening force and the bending moment is also derived. Finally, the modal frequencies of the rotor under different pretightening forces are obtained by the three-dimensional finite element method and the experimental modal method, respectively. Comparing the experimental test results with the calculated results, it is found that the double fractal model is reasonable to calculate the contact stiffness of the rod-fastened rotor.

2. Theoretical Analysis

2.1. The Experimental Rod-Fastened Rotor. The experimental rod-fastened rotor consists of discs, a front shaft end, a rear shaft end, and nine tie rods (see Figure 2). The rotor is clamped together by the circumferentially arranged tie rods. A rough contact interface is existed between two discs of the rotor. As shown in Figure 3, there are six rough contact interfaces of C1–C6 in the rotor. The structure of the rotor is bilaterally symmetrical. The material of the rotor is 40Cr.

The elastic modulus E is 206 GPa, the density ρ is 7870 kg/m³, and the Poisson ratio ν is 0.3.

2.2. The Mechanical Model of the Contact Segment in the Experimental Rod-Fastened Rotor. There are some contact asperities on the rough contact interface. The asperities come into contact under the pretightening force F_{pre} . According to the fractal model, a small plastic contact point first appears on the contact interface. As the pretightening force increases, the small plastic contact points merge into large contact points. When the contact area exceeds the critical value, the large contact points begin to make elastic contact. As shown in Figure 4, each asperity on the rough contact interface can be seen as a spring with bending stiffness, and all asperities on the contact interface can be characterized by a spring with equivalent flexural stiffness K_{cc} . Then, the equivalent flexural stiffness K_{eq} of the contact segment is a series connection of the flexural stiffness K_{cc} of the contact interface and the flexural stiffness K_s of the continuous shaft with the length L_s . K_{eq} is given by

$$K_{eq} = \left(\frac{1}{K_s} + \frac{1}{K_{cc}} \right)^{-1} = \frac{K_{cc}K_s}{K_{cc} + K_s}. \quad (1)$$

For the continuous shaft with the length L_s , the flexural stiffness is

$$K_s = \frac{EI}{L_s}, \quad (2)$$

where E is the elastic modulus, I is the moment of inertia, and L_s is the length of the contact segment.

Considering the effect K_{cc} on the K_{eq} , the flexural stiffness correction factor of the contact segment η is introduced by

$$\eta = \frac{K_{eq}}{K_s} = \frac{K_{cc}}{K_{cc} + K_s}. \quad (3)$$

The flexural stiffness correction coefficient η represents the stiffness reduction of the contact interface to the continuous shaft. For the contact segment, η is mainly related to the pretightening force and the bending moment.

2.3. The Equivalent Flexural Stiffness of the Contact Interface K_{cc}

2.3.1. The Double Fractal Model of the Contact Interface in the Experimental Rod-Fastened Rotor. A rough surface profile with double fractal characteristic can be represented by Weierstrass–Mandelbrot (W-M) function [16]:

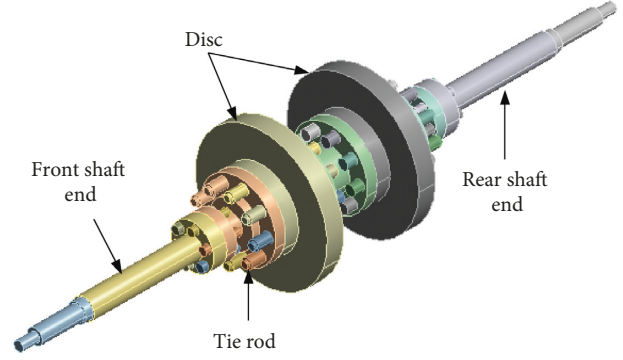
$$z(x) = L \left(\frac{G_1}{L} \right)^{D_1-1} \sum_{n=0}^{n_c} \cos(2\pi\gamma^n x L^{-1}) \gamma^{(D_1-2)n} + L \left(\frac{G_2}{L} \right)^{D_2-1} \sum_{n=0}^{n_{max}} \cos(2\pi\gamma^n x L^{-1}) \gamma^{(D_2-2)n}, \quad (4)$$

where L is the sampling length, G_1 and G_2 are the fractal roughness parameters which determine the profile height, D_1 and D_2 are the fractal dimensions of the surface topography ($1 < D_1 < 2$, $1 < D_2 < 2$), which determine the distribution ratio of high frequency and low frequency in the surface contour height, and γ is the contour spectral density.

The contact interfaces of the experimental rod-fastened rotor are machined by grinding, and the rough contact



(a)



(b)

FIGURE 2: The structure of the experimental rod-fastened rotor. (a) The machining model of the experimental rod-fastened rotor. (b) The three-dimensional model of the experimental rod-fastened rotor.

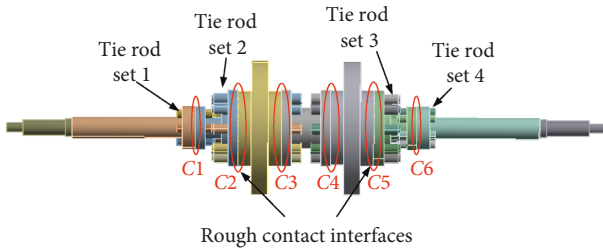


FIGURE 3: The rough contact interfaces of the experimental rod-fastened rotor.

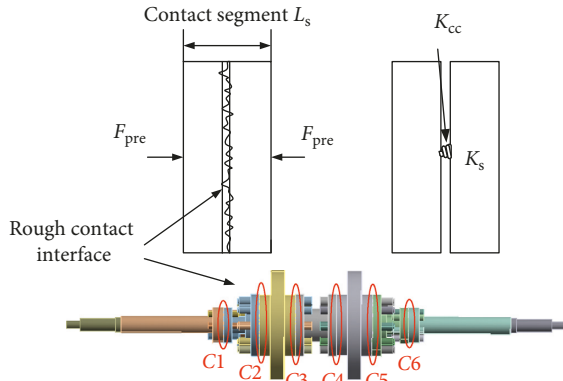


FIGURE 4: The contact segment of the experimental rod-fastened rotor.

interfaces can be regarded as isotropic. The contour curves of the contact interfaces are measured by the SJ201P surface topographer. According to the contour curve, the fractal parameters can be obtained by the structural function method.

When $\tau \leq \tau_{12}$, the structural function of the W-M function is

$$\begin{aligned} S_1(\tau) &= \langle [z(x) - z(x + \tau)]^2 \rangle \\ &= C_1 G_1^{2D_1 - 2} \tau^{4 - 2D_1}. \end{aligned} \quad (5)$$

When $\tau \geq \tau_{12}$, the structural function of the W-M function is

$$\begin{aligned} S_2(\tau) &= \langle [z(x) - z(x + \tau)]^2 \rangle \\ &= C_2 G_2^{2D_2 - 2} \tau^{4 - 2D_2}, \end{aligned} \quad (6)$$

where τ is the displacement along the x direction, C_1 and C_2 are the coefficients related to the fractal dimension, and $\langle \rangle$ indicates spatial average. The structural function diagram of the contour curve is shown in Figure 5. The structural function diagram is divided into two parts according to τ_{12} which represents the boundary displacement of the two fractal regions along the x direction. The region I corresponds to the fractal structure formed by the microfracture of the smaller scale, and the region II corresponds to the fractal structure formed by the plastic deformation of the larger scale. The contact of two rough surfaces can be equivalent to the contact between a rough face and a rigid face, and the structural function is the sum of the two rough face structure functions. According to the structural function diagram, the fractal parameters of the contact interface are obtained and shown in Table 1.

2.3.2. The Contact Model of the Double Fractal Surface.

The contact of two rough surfaces can be equivalent to the contact between a rough face and a rigid face. Figure 6 shows the microcontact established between an asperity of the rough surface and opposing rigid plane. The contact asperity is assumed to be a sphere, when the small contact asperities are in the state of full plastic.

Deformation of the normal contact force is given by

$$F_p = Ha, \quad (7)$$

where H is the hardness value of the material, $H = (2Y/3)\{1 + \ln[E/(2(1-\nu)Y)]\}$, Y is the yield stress, E is the elastic modulus, ν is the Poisson ratio, and $a = \pi(r_t)^2$ is the truncated area of the contact asperity, r_t is the radius of the truncated area.

When the pretightening force is increased, the small contact asperities are merged into a large contact asperity, and the large contact asperity begins to make elastic contact. When $a_t \leq a_c$, the contact interface is in a fully plastic contact state. When $a_t > a_c$, the contact interface enters the elastic-

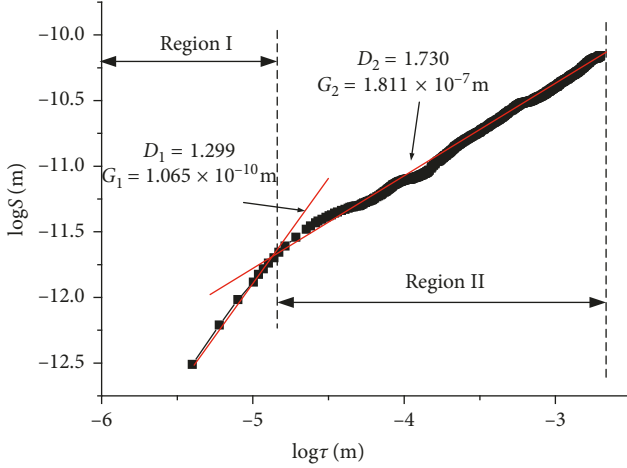


FIGURE 5: The structural function diagram of the contact interface contour curve.

TABLE 1: The fractal parameter values of the contact interface.

D_1	D_2	G_1 (m)	G_2 (m)	τ_{12} (m)	R_e (μm)
1.299	1.730	1.065×10^{-10}	1.811×10^{-7}	2.80×10^{-5}	1.57

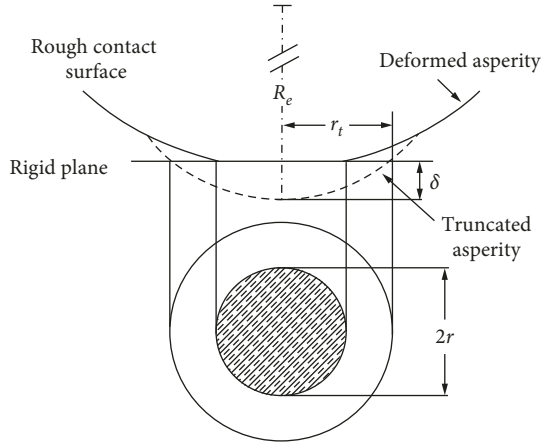


FIGURE 6: Schematic of a microcontact established between an asperity of composite rough surface and opposing rigid plane.

plastic contact state, where a_L is the truncated area of the maximum contact asperity and a_c is the critical truncated area where the elastic contact occurs.

For the contact asperity, the normal deformation δ can be expressed as [17]

$$\delta = 2G^{(D-1)} (\ln \gamma)^{1/2} (2r_t)^{(2-D)}. \quad (8)$$

According to the Hertz contact theory, the normal elastic force of a single contact asperity can be expressed as

$$F_e(\delta) = \frac{4E^* R_e^{1/2} \delta^{3/2}}{3}, \quad (9)$$

where E^* is the equivalent elastic modulus.

$$E^* = \left[\frac{(1-\nu_1^2)/E_1 + (1-\nu_2^2)}{E_2} \right]^{-1}, \quad (10)$$

where ν_1 , ν_2 and E_1 , E_2 are Poisson's ratio and elastic modulus of the contact interfaces, respectively. Because the same material is used for each part of the experimental rod-fastened rotor, $E_1 = E_2 = E$ and $\nu_1 = \nu_2 = \nu$.

In Figure 6, the relationship between r_t and δ is

$$(R_e - \delta)^2 + r_t^2 = R_e^2, \quad (11)$$

where the radius of curvature R_e is general much larger than δ . Then, equation (11) can be expressed as

$$r_t^2 = 2R_e \delta. \quad (12)$$

Substituting equations (8) and (12) into (9) yields

$$F_e(\delta) = \frac{2^{(9-2D)/2}}{3\pi^{(3-D)/2}} (\ln \gamma)^{1/2} G^{(D-1)} E^* a^{(3-D)/2}. \quad (13)$$

The critical truncated area a_c is given by [17]

$$a_c = \left[\frac{2^{(9-2D)} \pi^{(D-3)} G^{(2D-2)} \ln \gamma \left(\frac{E^*}{H} \right)^2}{9} \right]^{1/(D-1)}. \quad (14)$$

For the double fractal contact interface, region I is corresponding to the critical truncated area a_{c1} , region II is corresponding to the critical truncated area a_{c2} , and the boundary displacement τ_{12} corresponds to the truncated area a_{12} . The asperities deformation of the double fractal area can be divided into four cases according to the relationship among a_{c1} , a_{c2} , and a_{12} :

Case 1: when $a_{c1} < a_{c2}$, the contact asperities satisfying $a < a_{c1}$ in region I are plastic deformation, and the contact asperities satisfying $a_{c1} < a < a_{12}$ are elastically deformed.

Case 2: when $a_{c1} > a_{12}$, all contact asperities in region I are plastically deformed.

Case 3: when $a_{c2} < a_{12}$, all contact asperities in region II are elastically deformed.

Case 4: when $a_{c2} > a_{12}$, the contact asperities satisfying $a_{12} < a < a_{c2}$ in region II are plastically deformed, and the contact asperities satisfying $a > a_{c2}$ are in the elastic deformation state.

According to the fractal parameter values of the double fractal contact interface listed in Table 1, the value of truncated areas a_{c1} , a_{c2} , and a_{12} can be obtained, respectively, and the relationship is $a_{12} < a_{c2} < a_{c1}$. According to the relationship, the double fractal area of the contact interface satisfies the case 2 and case 4.

For the truncated area a_L of the maximum contact asperity, when $a_L < a_{12}$, the frequency distribution function of the contact asperities is given by [18]

$$n_1(a) = \frac{D_1}{2} \frac{(a_L)^{D_1/2}}{(a)^{(D_1+2)/2}}, \quad (a < a_{12}). \quad (15)$$

When $a_L > a_{12}$, the frequency distribution function of the contact asperities is expressed as

$$n_1(a) = \frac{D_1}{2} \left(\frac{a_L}{a_{12}} \right)^{D_2/2} \frac{(a_{12})^{D_1/2}}{(a)^{(D_1+2)/2}}, \quad (a < a_{12}), \quad (16)$$

$$n_2(a) = \frac{D_2}{2} \frac{(a_L)^{D_2/2}}{(a)^{(D_2+2)/2}}, \quad (a_{12} < a < a_L).$$

The total normal contact force of the contact interface F_N is the sum of the plastic contact force and the elastic contact force of the two regions. F_N can be expressed as

$$F_N = \int_0^{a_{12}} F_p n_1(a) d(a) + \int_{a_{12}}^{a_L} F_p n_2(a) d(a) + \int_{a_{12}}^{a_L} F_e n_2(a) d(a). \quad (17)$$

F_N is determined by the pretightening force F_{pre} . Combining with equation (17), a_L can be obtained. It will be applied to the following contact stiffness calculation.

2.3.3. The Flexural Stiffness of the Contact Interface of the Experimental Rod-Fastened Rotor. From the Hertz contact theory, the normal contact stiffness of each microcontact pair can be written as

$$k_n = \frac{dF_e(\delta)}{\delta}. \quad (18)$$

Neglecting the contact stiffness of the asperities in the state of plastic deformation, the normal contact stiffness K_n of the entire contact interface is equal to the sum of the normal contact stiffness of all elastic contact pairs of the contact interface. The contact stiffness K_n can be expressed as

$$K_n = \int_{a_{c2}}^{a_L} k_n n_2(a) d(a). \quad (19)$$

The value of K_n can be obtained by the method of numerical integration. For the annulus contact interface, the flexural stiffness of contact interface K_{cc} can be given by

$$K_{cc} = \iint_A \frac{K_n}{A} y^2 dA, \quad (20)$$

where A is the nominal contact area of the contact interface and y is the distance along the axis.

The value of K_{cc} is determined by the normal contact stiffness per unit area k_{n0} and the contact area. Since k_{n0} is a function of the contact pressure P , K_{cc} also can be expressed as

$$K_{cc} = \iint_A k_{n0}(P) y^2 dA. \quad (21)$$

As shown in Figure 7, the contact interface of the rod-fastened rotor is a concentric annular surface and the outer and inner radius of the annulus are R_1 and R_2 , respectively. When the contact interface is in the full contact state, the contact pressure is a linear function of y , then

$$P(y) = ay + b, \quad (22)$$

where a and b are the constant coefficients.

The rod-fastened rotor is subjected to the pretightening force and the bending moment during the operation. When

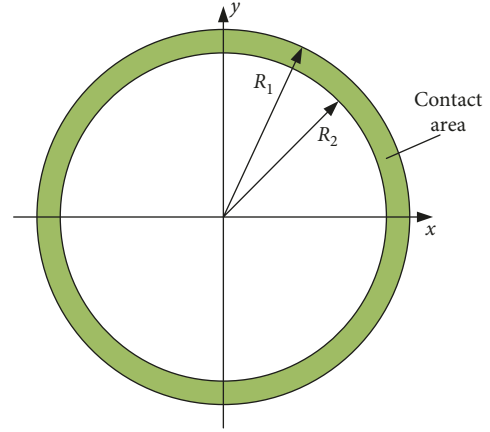


FIGURE 7: Schematic for the contact interface.

the pretightening force F_{pre} and the bending moment M are applied on the rod-fastened rotor, F_{pre} and M can be written as

$$F_{pre} = \iint_A P(y) dA = \iint_A (ay + b) dA = aS_x + bA, \quad (23)$$

$$M = \iint_A P(y) y dA = \iint_A (ay + b) y dA = aI + bS_x, \quad (24)$$

where $S_x = Ay_c$ is the static moment of the contact interface and y_c is the coordinate of the centroid. Combining equations (23) and (24), the coefficients a and b can be obtained. Substituting them into equation (22) yields

$$P(y) = \frac{M - P_0 S_x}{AI - S_x^2} (Ay - S_x) + P_0, \quad (25)$$

where $P_0 = F_{pre}/A$.

When the whole zone of the contact interface is in full contact, $y_c = 0$. Equation (25) can be written as

$$P(y) = P_0 (1 + \xi \beta), \quad (26)$$

where ξ is the flexural dimensionless load coefficient, $\xi = MR_1/IP_0$, and $\beta = y/R_1$.

For the annulus contact interface,

$$dA = 2\sqrt{R_1^2 - y^2} dy. \quad (27)$$

Combining equations (21) and (27), the K_{cc} is expressed as

$$K_{cc} = 2R_1^4 \int_{-1}^1 k_{n0}(P) \beta^2 \sqrt{1 - \beta^2} d\beta. \quad (28)$$

3. Application of Results and Validation

3.1. Equivalent Flexural Stiffness K_{eq} of the Contact Segment. The flexural stiffness K_{cc} of the contact interface in the experimental rod-fastened rotor can be obtained by the above calculation method. Combining with equation (1), the equivalent flexural stiffness of the contact segment K_{eq} can be obtained. K_{eq} will be affected by the pretightening force,

the bending moment, the contact area, and the length of the contact segment. To analyze the effect of above factors on K_{eq} , the contact segment corresponding to the contact interface C2 is selected to conduct the analysis.

3.1.1. Effect of the Pretightening Force and the Bending Moment on K_{eq} . The pretightening force and the bending moment applied on the experimental rod-fastened rotor will affect the contact pressure of the contact interface. In equation (26), the flexural dimensionless load coefficient ξ is introduced to represent the influence of the pretightening force and the bending moment. The effect of the contact interface on K_{eq} is denoted by the flexural stiffness correction coefficient η (see equation (3)). For the contact interface C2, the value of R_1 and R_2 is 110 mm and 70 mm, respectively. The nominal contact pressure P_0 can be obtained under different pretightening forces. Figure 8 shows the effect of the pretightening force and the bending moment on η . When ξ is constant, η increases with P_0 , but the increasing trend gradually slows down. When P_0 is constant, η decreases with the increase of ξ , which indicates that the contact interface will appear to be separated with the increase of the bending moment.

3.1.2. Effect of the Contact Area on K_{eq} . According to equation (28), the flexural stiffness K_{cc} is also influenced by the contact area. The outer radius R_1 is given as 110 mm, and the ratio of the inner radius and outer radius $\alpha = R_2/R_1$ is defined. The change of the contact area is obtained by changing α . Figure 9 shows the effect of the contact area on η . When ξ is constant, η increases with the decrease of α , indicating that the bending moment weakens against the bending stiffness with the increase of the contact area.

3.1.3. Effect of the Length of Contact Segment L_s on K_{eq} . According to equations (1) and (3), η is influenced by the length L_s of the contact segment. As shown in Figure 10, when L_s is small, the length of the contact segment has a greater influence on η . When L_s reaches a certain value, η no longer increases with L_s . Therefore, it is necessary to select the appropriate length of the contact segment during the calculation. In this paper, L_s is equal to 50 mm.

3.2. Modal Analysis of the Experimental Rod-Fastened Rotor. The modal analysis of the rotor is conducted, considering the effect of the contact stiffness. In this paper, the effect of the contact interface on the flexural stiffness is simulated by modifying the elastic modulus of the contact segment. According to equation (3), the flexural stiffness correction coefficient η is obtained. Then,

$$E_{eq} = \eta E, \quad (29)$$

where E_{eq} is the equivalent elastic modulus of the contact segment.

The modal analysis is performed, considering the effect of the pretightening force and the gravity bending moment. There are six contact segments in the experimental rod-

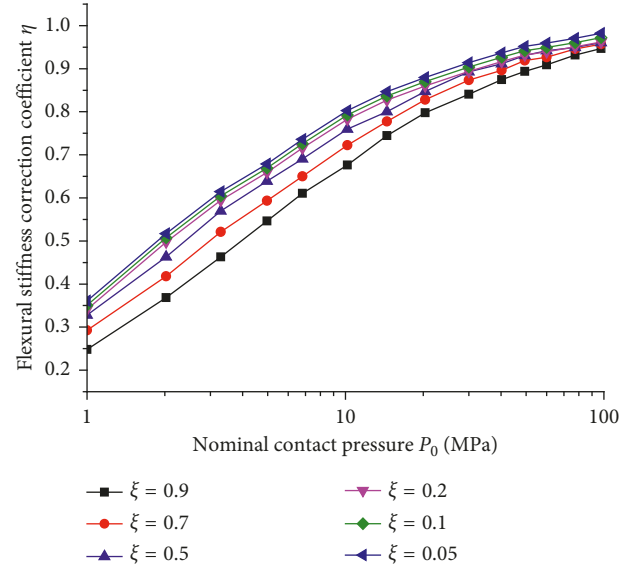


FIGURE 8: Effect of the pretightening force and the bending moment on η .

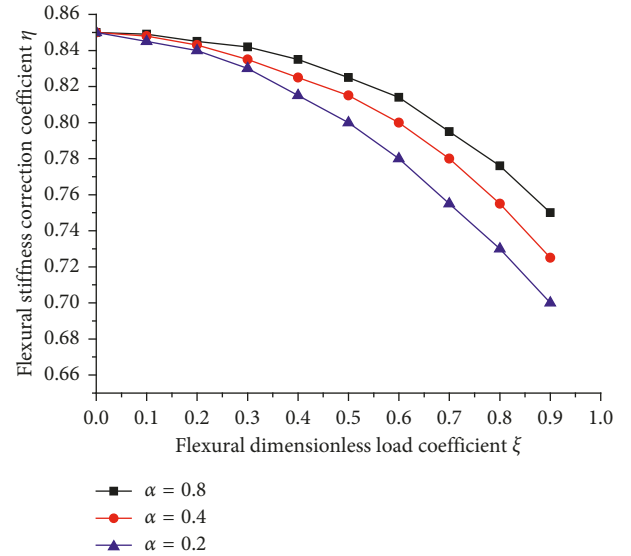


FIGURE 9: Effect of the contact area on η .

fastened rotor (see Figure 3). Due to the bilateral symmetrical structure, we only change the pretightening forces corresponding to tie rod set 2 and tie rod set 3, and the pretightening force of tie rod set 2 is equal to that of tie rod set 3. The pretightening forces corresponding to tie rod set 1 and tie rod set 4 are kept equal and constant. The different pretightening forces applied on the rotor are listed in Table 2.

The distribution of the gravity bending moment of the experimental rod-fastened rotor is shown in Figure 11. The distribution of the gravity bending moment is bilaterally symmetric. The gravity bending moments corresponding to the positions of C2 and C3 are selected as the bending moments of the contact interfaces. The length L_s of the two contact segments is both 50 mm. According to the

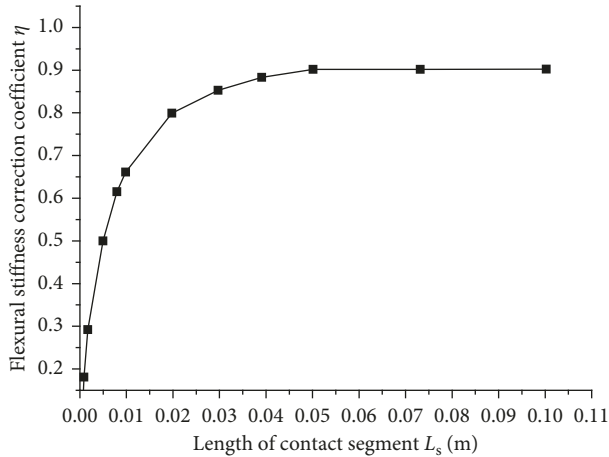


FIGURE 10: Effect of the length of the contact segment on η .

TABLE 2: Different pretightening forces applied on the tie rod set 2 and tie rod set 3.

Case	Pretightening force, F_{pre} (N)	Nominal contact pressure, P_0 (MPa)
1	33750	1.492
2	56250	2.487
3	113400	5.013
4	228600	10.106
5	282186	12.475

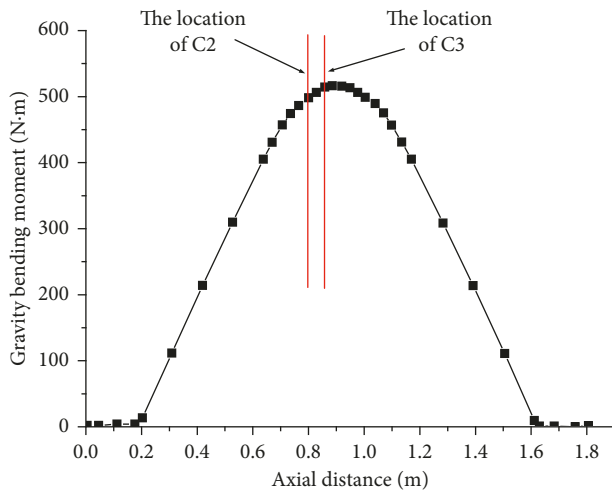


FIGURE 11: Distribution of the gravity bending moment of the experimental rod-fastened rotor.

pretightening force listed in Table 2, the flexural stiffness correction coefficients η of the two contact segments are listed.

As shown in Table 3, η increases with the pretightening forces.

The modal analysis of the experimental rod-fastened rotor is conducted using ANSYS Version 11.0. The block Lanczos method is applied to solve the modal analysis. The three-dimensional finite element model is shown in

Figure 12. The first five flexural mode shapes of the experimental rod-fastened rotor are shown in Figure 13. It can be seen that the first five mode shapes are mainly the vibration of the front and rear shaft ends, and the mode shapes of the discs are not obvious. Table 4 shows the calculated values of the first five orders of modal frequencies of the experimental rod-fastened rotor under different pretightening forces. As the pretightening force increases, the modal frequency of the rotor gradually increases. Meanwhile, the influence of the pretightening force on the 3rd and 5th order modal frequencies is greater than that of other orders. This can be explained from the mode shapes of the rotor in Figure 13. Since the 3rd and 5th order mode shapes of the discs are larger than the other orders, the frequencies of the 3rd and 5th order are more sensitive to the change of the contact stiffness.

3.3. Experiment Validation. To validate the calculation method considering the pretightening force and the bending moment, a simplified experimental rod-fastened rotor is manufactured (see Figure 2(a)), and the modal experiment is conducted. The multipoint exciting method is used to measure the modal parameters of the rotor. The rotor is excited by the force hammer. An acceleration sensor is used to acquire the response signals. The range of the measured frequency is 0–3200 Hz with a frequency resolution of 1.25 Hz. The measurement system is shown in Figure 14.

In order to verify the calculated results, the pretightening forces applied on the experimental rotor are set according to Table 2. In order to reflect the effect of gravity bending moment, the experimental rotor is suspended by an elastic wire rope. The experimental results of the first five orders of modal frequencies are shown in Table 5. The comparison between the calculated and experimental results is shown in Figure 15. It can be seen that the modal frequencies gradually increase with the nominal contact pressure P_0 , and the change trend of the calculated results is consistent with that of the experimental results. For the 3rd order and the 5th order, the difference between the calculated and experimental results is large. Because the 3rd and 5th order mode shapes of the discs are larger than the other orders, the frequencies of the 3rd and 5th order are more sensitive to the change of the contact stiffness, which is determined by the pretightening force.

The relative errors between the calculated and experimental results are listed in Table 6. For the 3rd and 5th order, the relative errors are large when the nominal contact pressure P_0 (pretightening force) is small. It could be explained by the relative errors of pretightening forces applied on the rotor being large when the pretightening forces are small. With the increase of P_0 , the relative errors decreased. According to the results of relative errors, it is found that the calculated results are correct.

4. Conclusions

In this paper, the contact stiffness of the rod-fastened rotor is analyzed considering the pretightening force and the bending moment. The results are summarized below:

TABLE 3: Flexural stiffness corrections under different pretightening forces.

Contact interface	Gravity bending moment (N·m)	Flexural stiffness correction coefficient, η				
		Case 1	Case 2	Case 3	Case 4	Case 5
C2	492	0.3421	0.4286	0.5657	0.6079	0.7522
C3	512	0.3377	0.4276	0.5654	0.6075	0.7520



FIGURE 12: Three-dimensional finite element model of the experimental rod-fastened rotor.

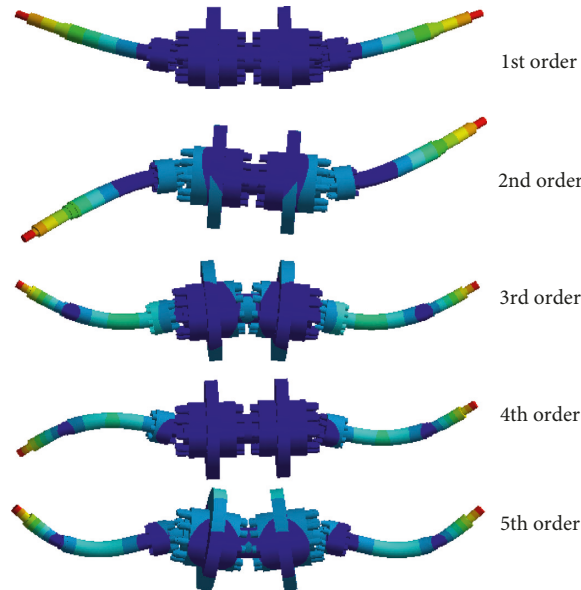


FIGURE 13: The first five flexural mode shapes of the experimental rod-fastened rotor.

TABLE 4: Calculated results of flexural vibration modal frequencies of the experimental rod-fastened rotor.

Case	Pretightening force (N)	Nominal contact pressure, P_0 (MPa)	Dimensionless load coefficient, ξ (C2)	1st order (Hz)	2nd order (Hz)	3rd order (Hz)	4th order (Hz)	5th order (Hz)
1	33750	1.492	0.377	145.40	206.85	574.38	730.45	876.57
2	56250	2.487	0.226	145.66	206.99	577.77	731.33	880.96
3	113400	5.013	0.112	145.89	207.12	580.84	732.03	885.13
4	228600	10.106	0.055	146.04	207.19	582.78	732.50	891.86
5	282186	12.475	0.045	146.31	207.25	584.58	732.91	892.90

(1) The double fractal model and Hertz contact theory are used to calculate the normal contact stiffness of the contact interface. The effect of the pretightening force, the bending moment, the contact area, and the length of the contact segment on the equivalent flexural stiffness K_{eq} are analyzed. When the flexural dimensionless load coefficient ξ is constant, the flexural stiffness correction coefficient η increases with the nominal contact pressure P_0 (pretightening

force), but the increasing trend gradually slows down.

When P_0 is constant, η decreases with the increase of ξ , which indicates that the contact interface will appear to be separated with the increase of the bending moment.

(2) The calculated and experimental modal analysis is conducted considering the pretightening force and

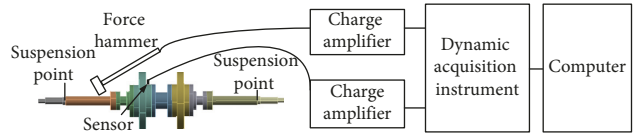


FIGURE 14: The modal measurement system.

TABLE 5: Experimental results of flexural vibration modal frequencies of the experimental rod-fastened rotor.

Case	Pretightening force (N)	Nominal contact pressure, P_0 (MPa)	Dimensionless load coefficient, ξ (C2)	1st order (Hz)	2nd order (Hz)	3rd order (Hz)	4th order (Hz)	5th order (Hz)
1	33750	1.492	0.377	143.5	204.8	546.3	723.1	821.3
2	56250	2.487	0.226	144.4	205.6	557.5	725.0	838.8
3	113400	5.013	0.112	146.9	206.9	569.4	733.1	848.1
4	228600	10.106	0.055	147.5	207.5	573.8	736.3	864.4
5	282186	12.475	0.045	148.1	208.2	578.5	737.9	884.8

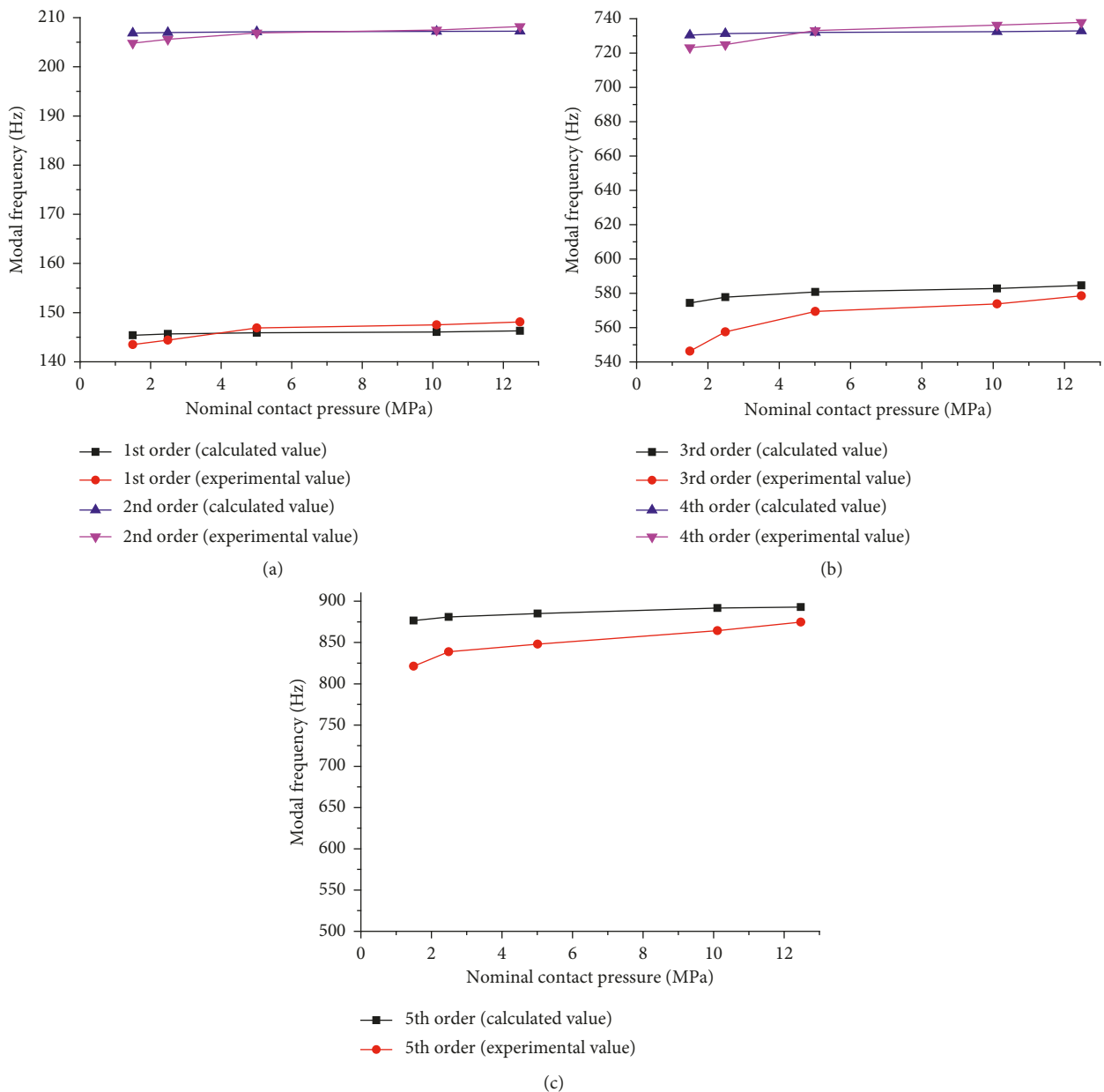


FIGURE 15: The comparison of modal frequency between the calculated and experimental results. (a) 1st and 2nd order modal frequency. (b) 3rd and 4th order modal frequency. (c) 5th order modal frequency.

TABLE 6: Relative errors between the calculated and experimental results.

Nominal contact pressure, P_0 (MPa)	1.492	2.487	5.013	10.106	12.475	
Dimensionless load coefficient, ξ (C2)	0.377	0.226	0.112	0.055	0.045	
Relative error (%)	1st order	1.31	0.87	-0.69	-1.00	-1.22
	2nd order	0.99	0.67	0.11	-0.15	-0.46
	3rd order	4.89	3.51	1.97	1.54	1.04
	4th order	1.01	0.87	0.15	0.52	0.68
	5th order	6.31	4.79	4.18	3.08	0.91

the bending moment (due to gravity). As P_0 increases, the modal frequencies increase, and the experimental results are consistent with the calculated results. Therefore, the double fractal model is reasonable to calculate the contact stiffness of the rod-fastened rotor.

Data Availability

The data used to support the findings of this study are included within the article.

Conflicts of Interest

The authors declare that they have no conflicts of interest.

Acknowledgments

This work was supported by the National Nature Science Foundation of China (no. 11872289) and the Key Project of Natural Science Foundation of Xi'an Jiaotong University (no. zrz2017025).

References

- [1] N. Klompas, "Effects of anomalous rotor joints on turbo-machine dynamics," *Journal of Engineering for Power*, vol. 105, no. 4, pp. 927–934, 1983.
- [2] A. S. Lee and Y. S. Lee, "Rotordynamic characteristics of an APU gas turbine rotor-bearing system having a tie shaft," *KSME International Journal*, vol. 15, no. 2, pp. 152–159, 2011.
- [3] M. J. Lu, H. P. Geng, B. S. Yang et al., "Finite element method for disc-rotor dynamic characteristics analysis of gas turbine rotor considering contact effects and rod preload," in *Proceedings of the 2010 IEEE International Conference on Mechatronics and Automation*, pp. 1179–1183, Tianjin, China, August 2010.
- [4] H. Liu, C. Li, W. M. Wang et al., "Nonlinear dynamic analysis of a flexible rod fastening rotor bearing system," *Journal of Mechanical Engineering*, vol. 46, no. 19, p. 53, 2010.
- [5] Z. S. Rao, S. B. Xia, and G. M. Wang, "A study of contact stiffness of flat rough surfaces," *Journal of Mechanical Strength*, vol. 16, no. 3, pp. 72–75, 1994.
- [6] P. He, Z. S. Liu, and G. L. Wang, "Rotor dynamic analysis of tie-bolt fastened rotor based on elastic-plastic Contact," *Proceedings of the ASME Turbo Expo 2011*, vol. 6, pp. 365–373, 2011.
- [7] Y. C. Zhang, Z. G. Du, L. M. Shi et al., "Determination of contact stiffness of rod-fastened rotor based on modal test and finite element analysis," *Journal of Engineering for Gas Turbines and Power*, vol. 132, no. 9, pp. 47–49, 2010.
- [8] A. A. M. Isa, J. E. T. Penny, and S. D. Garvey, "The dynamics of bolted and laminated rotors," *Proceedings of the Society of Photo-Optical Instrumentation Engineers*, vol. 4062, pp. 867–872, 2000.
- [9] J. Gao, Q. Yuan, P. Li et al., "Effects of bending moments and pre-tightening forces on the flexural stiffness of contact interfaces in rod-fastened rotors," *Proceedings of ASME Turbo Expo 2012*, vol. 9, pp. 511–519, 2012.
- [10] T. F. Lehnhoff, K. I. Ko, and M. L. McKay, "Member stiffness and contact pressure distribution of bolted joints," *Journal of Mechanical Design*, vol. 116, no. 2, pp. 550–557, 1994.
- [11] T. F. Lehnhoff and B. A. Bunyard, "Effects of bolt threads on the stiffness of bolted joints," *Journal of Pressure Vessel Technology*, vol. 123, no. 2, pp. 161–165, 2001.
- [12] S. X. Yuan, Y. Y. Zhang, Y. S. Zhu et al., "Study on the equivalent stiffness of heavy-duty gas turbines composite rotor with curvic couplings and spindle tie-bolts," *ASME 2011 Power Conference*, vol. 1, pp. 567–576, 2011.
- [13] L. He and J. Zhu, "The fractal character of processed metal surfaces," *Wear*, vol. 208, no. 1-2, pp. 17–24, 1997.
- [14] S. Y. Jiang, Y. J. Zheng, and H. Zhu, "A contact stiffness model of machined plane joint based on fractal theory," *Journal of Tribology-Transactions of the ASME*, vol. 132, no. 1, pp. 1–7, 2010.
- [15] R. Buczkowski, M. Kleiber, and G. Starzynski, "Normal contact stiffness of fractal rough surfaces," *Archives of Mechanics*, vol. 66, no. 6, pp. 411–428, 2014.
- [16] A. Majumdar and C. L. Tien, "Fractal characterization and simulation of rough surfaces," *Wear*, vol. 136, no. 2, pp. 313–327, 1990.
- [17] W. Yan and K. Komvopoulos, "Contact analysis of elastic-plastic fractal surfaces," *Journal of applied physics*, vol. 84, no. 7, pp. 3617–3624, 1998.
- [18] B. Bhushan and A. Majumdar, "Elastic-plastic contact model for bifractal surfaces," *Wear*, vol. 153, no. 1, pp. 53–64, 1992.



Hindawi

Submit your manuscripts at
www.hindawi.com

